CHEMISTRY OF MATERIALS

ARTICLE

pubs.acs.org/cm

Atomic Structure of a Lithium-Rich Layered Oxide Material for Lithium-Ion Batteries: Evidence of a Solid Solution

Karalee A. Jarvis,[†] Zengqiang Deng,[†] Lawrence F. Allard,[‡] Arumugam Manthiram,[†] and Paulo J. Ferreira*[,†]

[†]Materials Science and Engineering Program, University of Texas at Austin, Austin, Texas 78712, United States

[‡]High Temperature Materials Laboratory, Materials Science & Technology Division, Oak Ridge National Laboratory, Oak Ridge, Tennessee 37831, United States

ABSTRACT: $Li[Li_{0.2}Ni_{0.2}Mn_{0.6}]O_2$, which is a cathode material for Li-ion batteries with enhanced capacity, has been examined, for the first time, with a combination of aberration-corrected scanning transmission electron microscopy (STEM), STEM computer simulations, and diffraction scanning transmission electron microscopy (D-STEM). These techniques, in combination with X-ray diffraction (XRD) and conventional electron diffraction (ED), indicate that this material is composed of a solid solution with $C2/m$ monoclinic symmetry and multiple planar defects. In addition, we show that XRD and ED alone can give misleading information and cannot resolve the structure of these materials without the additional use of the aforementioned techniques.

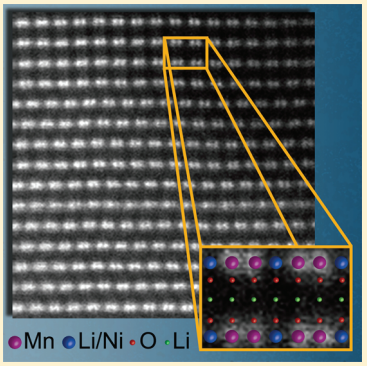

KEYWORDS: Li-ion batteries, nanostructures, characterization tools

INTRODUCTION

Lithium-ion batteries generally use layered $LiCoO_2$ or $LiNi_{1-y-x}Mn_yCo_xO_2$ as cathodes and graphite as the anode. However, these cathodes are limited in energy density, because of their reversible capacity values <200 mAh/g. With an aim to increase the energy density, the synthesis of novel materials composed of layered $Li[Li_{1/3}Mn_{2/3}]O_2$ (generally designated as Li_2MnO_3) and $LiMO_2$ have become appealing, because they exhibit much higher capacities (~250 mAh/g). These compositions can be represented as $Li[M_{1-x}Li_x]O_2$, where the elements in the brackets represent the composition of the transition-metal layer. It has been proposed that these $Li[M_{1-x}Li_x]O_2$ samples are composed of two phases, namely, a parent trigonal $LiMO_2$ phase (space group $R\bar{3}m$), and a monoclinic Li_2MnO_3 phase (space group $C2/m$).[1−4] The higher capacity of $Li[M_{1-x}Li_x]O_2$ is believed to be partially due to the monoclinic Li_2MnO_3 phase, which acts to stabilize the structure of the trigonal $LiMO_2$ phase during Li-extraction (charge).[2−5] On the other hand, some researchers believe that the two components, Li_2MnO_3 and $LiMO_2$, exist as a solid solution.[6,7] As a result, much debate has been spurred over the atomic structure of these materials and how they relate to the materials' electrochemical properties.

To address this issue, several research groups have used X-ray diffraction (XRD) and/or selected-area and convergent-beam electron diffraction (ED) techniques on various layered oxide cathodes.[1,4,6−18] However, the data obtained with these techniques have been interpreted differently by different groups. In terms of XRD results, many groups have concluded that the diffraction peaks in the range of 20°−35°, which are weak and broad, correspond to Li_2MnO_3 regions within a $LiMO_2$ matrix.[1,4,14] On the other hand, some claimed that these peaks result from long-rang Li ordering in the transition-metal layer and not the presence of Li_2MnO_3 regions.[6,7] Bréger et al.[7] show that care must be taken in interpreting XRD patterns as peak broadening and weakening can result from stacking faults and not from a loss of long-range ordering in the transition-metal layer. ED results have also led to different conclusions. Many researchers have interpreted extra spots and streaks in the ED patterns as superstructures and/or domains of Li_2MnO_3.[1,3,16] However, Boulineau et al.,[11] by studying Li_2MnO_3, suggested that the streaks and extra spots in ED patterns are due to stacking faults. Similar conclusions were made for two Li-rich layered oxide materials; however, these conclusions were not based solely on ED.[9,14,18] Weill et al.[17] have claimed that neither XRD nor ED can be used to concretely identify the crystal structure. Instead, these authors attribute line broadening in XRD and superlattice reflections and streaking in ED to either a structure with point defects and stacking changes along the c-axis, or a system with regions where ordered (Li_2MnO_3) and disordered ($LiMO_2$) domains coexist.

In the present work, the focus is on the compound $Li[Li_{0.2}Ni_{0.2}Mn_{0.6}]O_2$. Armstrong et al.[8] used neutron diffraction analysis to show that this material is primarily a trigonal $R\bar{3}m$ phase with Li_2MnO_3-like components. Lei et al.[14] also reported a trigonal $R\bar{3}m$ phase with ordering in the transition-metal layer, using XRD, ED, high-resolution transmission electron microscopy (HRTEM), and scanning transmission electron microscopy (STEM). Bareño et al.,[9] using ED and aberration-corrected STEM, showed that the $Li[Li_{0.2}Ni_{0.2}Mn_{0.6}]O_2$ material cannot be assigned as a single phase.

Received: March 22, 2011
Revised: June 1, 2011
Published: July 19, 2011

Table 1. Classification of Crystallographic Phases

crystal family	crystal system	required symmetries of point group	number of space groups	lattice system
monoclinic	monoclinic	one 2-fold axis of rotation and one mirror plane	13	monoclinic
hexagonal	trigonal	one 3-fold axis of rotation	7	rhombohedral
hexagonal	trigonal	one 3-fold axis of rotation	18	hexagonal
hexagonal	hexagonal	one 6-fold axis of rotation	27	hexagonal

The objectives of the current paper are i) clarify the aforementioned debate, by determining if the $Li[Li_{0.2}Ni_{0.2}Mn_{0.6}]O_2$ compound is composed of two separate phases, Li_2MnO_3 and $LiMO_2$, or whether it is a solid solution, ii) better understand the atomic arrangements of this material, and iii) determine which techniques can accurately determine the atomic structures. These objectives are critical for any future work trying to correlate the electrochemical behavior of lithium-rich layered oxides with local composition and structure.

To address this issue, we first used XRD and nanobeam electron diffraction (NBED) to characterize the material. However, as discussed above, these techniques may lead to different interpretations, and thus are not able to provide conclusive evidence regarding the crystal structure or phase analysis. Therefore, aberration-corrected high-angle annular dark-field (HAADF) STEM imaging was subsequently employed, which allowed us to examine the structure and composition at the atomic level. In order to more reliably interpret the HAADF-STEM images, computer simulations were also performed, using the optical parameters of the aberration-corrected electron microscope and compared with the experimental images. Finally, we employed a novel technique, diffraction scanning transmission electron microscopy (D-STEM),[19] recently developed in our laboratory, which allows us to collect electron diffraction maps from specific locations with a spatial resolution of 1−2 nm. This is the first time that this combination of techniques, namely XRD, aberration-corrected HAADF-STEM imaging, STEM image simulations, and D-STEM, has been used on layered oxide cathodes, allowing us to unambiguously determine the atomic structure of this material.

In order to facilitate the discussion to follow, it is important to define some of the crystallographic terminology that is used throughout the paper. So far, many different terms have been used in the literature to describe the $R\bar{3}m$ phase of these layered oxides, in particular, trigonal, rhombohedral, and hexagonal.[1,3,4,6,7,9−11,13,14,16,17,20−22] While none of these are incorrect, the different nomenclature used by various authors may lead to some confusion.

Table 1 shows the different terminology possible for the $R\bar{3}m$ and the $C2/m$ phases. The $R\bar{3}m$ phase can be categorized as hexagonal according to the crystal family, trigonal according to the crystal system, and rhombohedral according to the lattice system. However, since the hexagonal definition could indicate a 6-fold or a 3-fold axis of rotation while the trigonal nomenclature can only have a 3-fold axis of rotation, we will refer to the $R\bar{3}m$ phase as trigonal in this paper. On the other hand, the $C2/m$ space group exhibits one 2-fold axis of rotation and one mirror plane and, thus, belongs to the monoclinic crystal and lattice systems. In summary, this paper will use the crystal system classification (trigonal or monoclinic) to define the crystal structures, to avoid confusion and ambiguity.

Following the aforementioned nomenclature, $LiMO_2$, the parent structure, is reported to have a trigonal $R\bar{3}m$ structure (see Figure 1a).[4,6,16,21,22] In particular, its composition is a repeating sequence of a transition-metal layer, an oxygen layer, a lithium layer, an oxygen layer, and a transition-metal layer. The atoms in the transition-metal (M) layer, which correspond to the (001) plane, are arranged in a hexagonal pattern (see Figure 1b), where each atomic site (gray) has the same probability of being occupied by any M with no specific ordering. On the other hand, while Li_2MnO_3 has the same stacking sequence as $LiMO_2$ (Figure 2a), the transition-metal layer ($Li_{1/3}Mn_{2/3}$ or $LiMn_2$) orders, such that the excess Li occupies atomic sites S_1 (Figure 2b) and Li is surrounded by six Mn atoms on sites S_2.

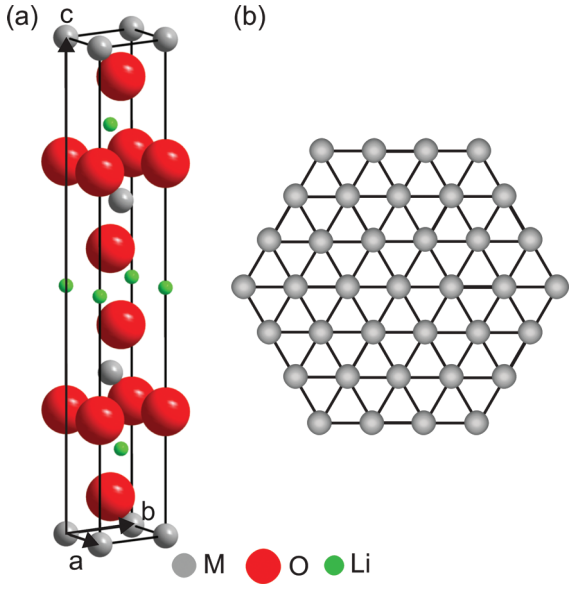

Figure 1. Trigonal ($R\bar{3}m$) $LiMO_2$ (a) unit cell and (b) atomic arrangement in the transition-metal layer. (The lattice parameters are $a = b = 2.8873$ Å, $c = 14.2901$ Å, $\alpha = \beta = 90°$, and $\gamma = 120°$.[16])

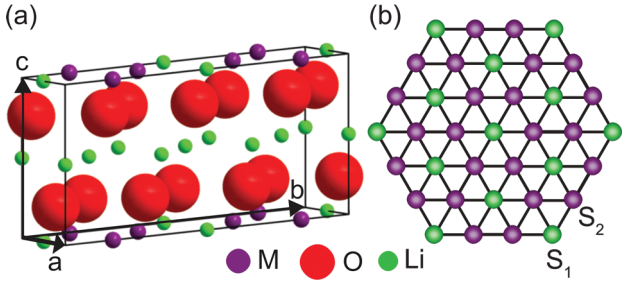

Figure 2. Monoclinic ($C2/m$) Li_2MnO_3 (a) unit cell and (b) atomic arrangement in the transition-metal layer. S_1 and S_2 indicate sites occupied, respectively, by excess Li atoms and Mn atoms. (The lattice parameters are $a = 4.937$ Å, $b = 8.532$ Å, $c = 5.030$ Å, $\alpha = \gamma = 90°$, and $\beta = 109.46°$.[23])

dx.doi.org/10.1021/cm200831c |Chem. Mater. 2011, 23, 3614–3621

This ordering reduces the symmetry to the monoclinic $C2/m$ unit cell.[4,7,10,11,15,23] This information is the basis for our characterization of the composition $Li[Li_{0.2}Ni_{0.2}Mn_{0.6}]O_2$ in order to determine the crystal structure and the phases present.

EXPERIMENTAL SECTION

The $Li[Li_{0.2}Ni_{0.2}Mn_{0.6}]O_2$ oxide was synthesized by a combined citric acid and EDTA (ethylenediamine tetraacetic acid) complexation route. EDTA and citric acid were first dissolved in NH_4OH and an aqueous solution containing required amounts of lithium, manganese, and nickel acetates were added to this solution. The citric acid:EDTA: metal ions molar ratio were optimized to be ~1.5: 1: 1. The mixed solution was then heated at ~120 °C under stirring until a viscous gel was obtained, which then heated first at ~250 °C and then at 850 °C for 5 h to get the final oxide powder.

The sample was characterized by XRD with a Philips X'pert diffractometer (with Cu Kα radiation). Data were collected in a step-scan mode in the range of 10°−110° with intervals of 0.03°. XRD computer simulations were carried out using Diamond 3.2e2 software with a wavelength of 1.5406 Å (Cu Kα).

Subsequently, the samples were sonicated or ground with a mortar and pestle in methanol and deposited onto lacy carbon grids. Upon sample preparation, NBED and D-STEM[19] were performed on a JEOL Model 2010F TEM system. The samples were imaged with a JEOL Model 2200FS TEM/STEM system that was equipped with a CEOS corrector for the illuminating lenses, and a high-angle annular dark-field (HAADF) detector. The instrument, located in the Advanced Microscopy Laboratory at Oak Ridge National Laboratory, was made available through the High Temperature Materials Laboratory's national user program. ED pattern simulations were carried out using the online software WebEmaps.[24]

To simulate the STEM images, atomic models, created in VESTA, were exported to HREM Simulation Suite, which is a TEM/STEM simulation software package based on the FFT Multislice technique.[25] The HREM Simulation Suite evaluates both the wave function and its Fourier transform at each slice, using the approximation by Weickenmeier and Kohl[26] to calculate the elastic scattering amplitude. This is a good approximation when considering electrons scattered at high angles, which is the geometry for recording HAADF images.[25] The HAADF intensity is then calculated by adding the thermal diffuse scattering factor to the elastic scattering amplitude.[25] This is important because atomic vibrations dampen the intensity of the electron waves going through the specimen. Microscope parameters corresponding to the settings used for the operation of the JEOL 2200FS aberration-corrected STEM at Oak Ridge National Laboratory were used. For all structures, the multislice simulations were carried out assuming a step scanning size of 0.2 Å (less than the distance to be resolved) and a minimum slice thickness of 1.0 Å. The Debye−Waller factor (B), which is related to the mean square of the thermal displacement of an atom from its equilibrium position, was acquired for each atomic position from the literature. For Li_2MnO_3, B was obtained from Strobel et al.[23] for each atomic position. These values were also used for the solid solution, since they have similar structures. For $Li[Mn_{0.5}Ni_{0.5}]O_2$, B was taken from Meng et al.[16] After the simulations were completed, the simulated images were compared with the actual STEM images for verification.

RESULTS AND DISCUSSION

XRD was first used to characterize the $Li[Li_{0.2}Ni_{0.2}Mn_{0.6}]O_2$ phase(s), and the results are shown in Figure 3. Most of the peaks can be indexed based on the $R\bar{3}m$ structure except for the peaks between 20° and 30°, which can only be indexed based on the monoclinic ($C2/m$) structure. On this basis, the material can be

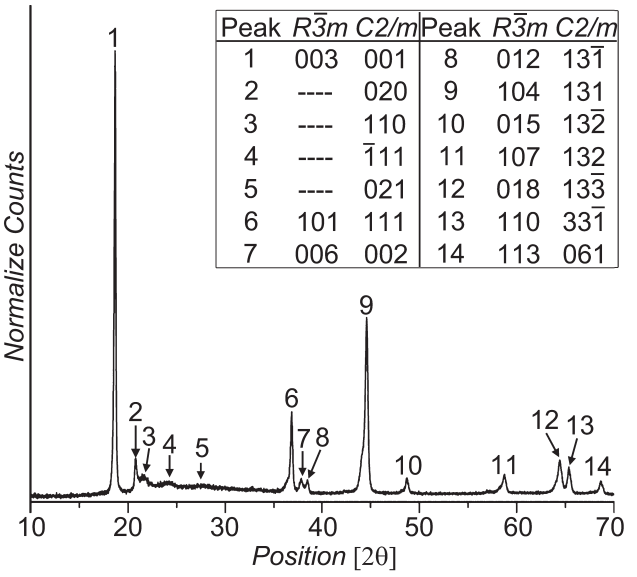

Peak	$R\bar{3}m$	$C2/m$	Peak	$R\bar{3}m$	$C2/m$
1	003	001	8	012	$13\bar{1}$
2	----	020	9	104	131
3	----	110	10	015	$13\bar{2}$
4	----	$\bar{1}11$	11	107	132
5	----	021	12	018	$13\bar{3}$
6	101	111	13	110	$33\bar{1}$
7	006	002	14	113	061

Figure 3. Experimental XRD pattern with major peaks numbered. The peaks are labeled according to $R\bar{3}m$ and $C2/m$ symmetry in the inset table. The dashes for peaks 2−5 in the $R\bar{3}m$ column indicate that there are no allowed reflections at these positions for the $R\bar{3}m$ space group.

characterized as a combination of two phases, namely, a trigonal $R\bar{3}m$ phase ($Li[Ni_{0.5}Mn_{0.5}]O_2$) and a monoclinic $C2/m$ phase (Li_2MnO_3) which, according to the stoichiometry, are in a 50:50 ratio. However, all the peaks indexed based on the $R\bar{3}m$ structure can also be indexed based on the $C2/m$ structure (see the table in Figure 3), which means that the $Li[Li_{0.2}Ni_{0.2}Mn_{0.6}]O_2$ compound can also be interpreted as a solid solution with $C2/m$ symmetry. Because the XRD data were inconclusive, additional X-ray simulations were performed to better understand the XRD pattern obtained.

While the atomic arrangements of the transition-metal layer are well-known for the two phases $LiMO_2$ ($R\bar{3}m$)[4,6,16,21,22] and Li_2MnO_3 ($C2/m$)[4,7,10,11,15,23] (Figure 4a), the atomic arrangement of the transition-metal layer for a $C2/m$ solid solution of $Li[Li_{0.2}Ni_{0.2}Mn_{0.6}]O_2$ is not well-known. Weill et al.[17] showed that, for $Li_{1.12}(Ni_{0.425}Mn_{0.425}Co_{0.15})_{0.88}O_2$, the larger cations ($Li^+$ and Ni^{2+}) prefer the S_1 sites, while the smaller cations (Ni^{3+}, Mn^{4+}, and Co^{3+}) prefer the S_2 sites, although they do not specify if the cations arrange on specific S_1 and S_2 sites. Lei et al.[14] reported the ordering of Li with respect to Mn in the transition-metal layer for $Li_{0.22}Ni_{0.17}Mn_{0.61}$. In addition, they indicated that Ni substitutes randomly for Li in the S_1 site. To resolve the structure of the $C2/m$ solid solution for this composition, several atomic models were considered for the X-ray simulations, keeping in mind that the transition-metal layer can assume various atomic arrangements of Mn, Li, and Ni (see Figure 4b).

The first possible atomic arrangement is a completely random distribution (disordered structure) of Li, Mn, and Ni, in which, according to stoichiometry, each atomic position has a 60% probability of being Mn, 20% probability of being Li, and 20% probability of being Ni. The second possible configuration in Figure 4b involves partial ordering in the transition-metal layer. In this case, Li is coordinated by six Mn atoms and, according to the transition-metal layer stoichiometry, ($Li_{(1/3)-(2/3)x}Ni_x Mn_{(2/3)-(1/3)x}$), 40% of the Li sites ($S_1$) as well as 10% of the Mn sites (S_2) are randomly replaced by Ni. As a result, partial

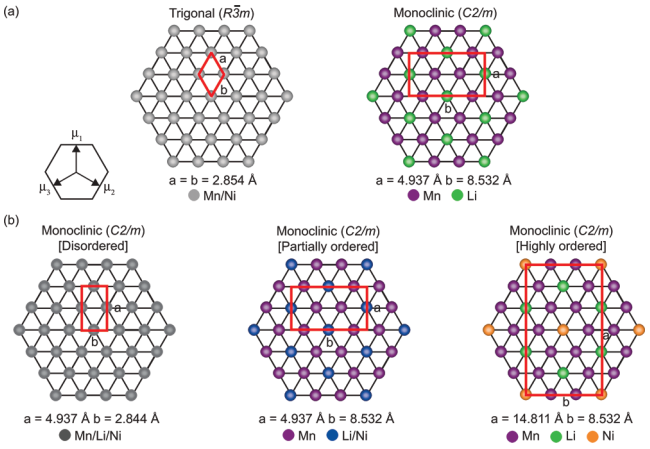

Figure 4. Atomic ordering in a single transition-metal layer of $Li[Li_{0.2}Ni_{0.2}Mn_{0.6}]O_2$ for (a) a two-phase system with a trigonal parent structure, $Li[Ni_{0.5}Mn_{0.5}]O_2$, and regions of a monoclinic phase, $Li[Li_{1/3}Mn_{2/3}]O_2$ (Li_2MnO_3), and (b) a solid solution with varying degrees of order. The lattice parameters (a and b) for each unit cell are shown. The atomic ratios for the light gray, dark gray, and blue sites are given as follows: light gray, 50% Mn and 50% Ni; dark gray, 60% Mn, 20% Ni, and 20% Li; and blue sites, 40% Ni and 60% Li. While not indicated in the legend, 10% of the Mn sites are occupied randomly by Ni for both the partially ordered and highly ordered model and 10% of the Li sites in the highly ordered model are occupied randomly by Ni. This will not change the unit-cell dimensions.

ordering results in a change of the lattice parameter b from 2.844 Å (disordered $C2/m$ structure) to 8.532 Å (partially ordered) (see Figure 4b), while the lattice parameters a and c remain the same compared with the disordered system. The final possible arrangement (Figure 4b) involves nickel ordering in specific S_1 sites in the transition-metal layer. Because of the $C2/m$ symmetry operations, it is not possible to completely order all the nickel in the S_1 sites while maintaining the $Li_{0.2}Ni_{0.2}Mn_{0.6}$ composition in the transition-metal layer. To resolve this issue, we have randomly replaced 10% of the Mn sites with Ni and 10% of the Li sites with Ni. We term this structure "highly ordered". While there are multiple ways of ordering the Ni in the lattice, we have chosen to order Ni such that the smallest unit cells are produced. In this case, the lattice parameter a increases to 14.81 Å, while b and c are maintained at 8.53 Å and 5.03 Å, when compared with the partially ordered $C2/m$ structure (Figure 4b). Any other arrangement of Ni will either increase the lattice parameters or maintain the same cell size.

Because of the increase in lattice parameters, the XRD peaks shift to lower angles (Figure 5). As a result, there are peaks at $2\theta < 18°$ for the highly ordered structure that do not match the experimental data. On the other hand, for the partially ordered $C2/m$ structure, the peak positions match very well with the experimental data. The absence of peaks between $20° < 2\theta < 30°$ do not match the experimental data for the fully disordered case. Therefore, we can conclude that, for the case of a solid solution, the composition $Li[Li_{0.2}Ni_{0.2}Mn_{0.6}]O_2$ should exhibit a partially ordered structure, which is similar to results reported by Lei et al.,[14] and $C2/m$ symmetry.

To this point, based on XRD data alone, the crystal structure of $Li[Li_{0.2}Ni_{0.2}Mn_{0.6}]O_2$ is either a combination of a disordered $R\bar{3}m$ structure with small $C2/m$ regions, or a single partially ordered $C2/m$ monoclinic phase. We next describe the results obtained by STEM imaging, ED, D-STEM, and image simulations, which provide critical additional information on the crystal structure.

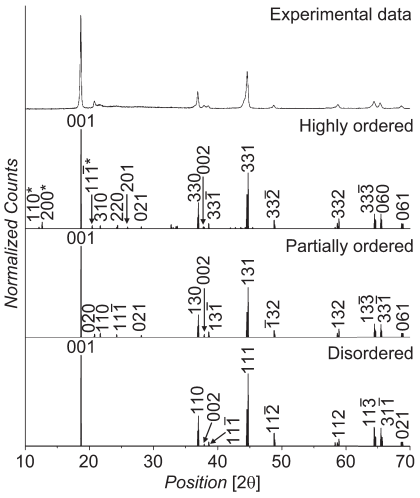

Figure 5. (a) Experimental XRD pattern for $Li[Li_{0.2}Ni_{0.2}Mn_{0.6}]O_2$ and simulated XRD patterns for the cases where the transition-metal layer is highly ordered, partially ordered, and disordered for a $C2/m$ structure. The asterisk (*) indicates peaks in the simulated XRD pattern that are absent in the experimental data.

In order to interpret the STEM images, it is important to understand that, for images of atomic columns in a crystal structure, the contrast has been shown to be directly related to the relative atomic number by a factor of $\sim Z^{1.7}$ (where Z is the atomic number).[27] As a result, the brighter regions in the STEM images correspond to areas with atomic columns that have higher average atomic number. In the case of $Li[Li_{0.2}Ni_{0.2}Mn_{0.6}]O_2$, the elements Mn and Ni have significantly higher masses than Li and O; therefore, atomic columns with high concentrations of these elements are expected to be brighter. Direct imaging of this material has been observed by Bareno et al.[9] and Lei et al.[14] They showed that, when the transition-metal planes are observed parallel to the electron beam and like atoms stack on top of each other, lithium ordering is revealed (a dark spot corresponding to the Li column, followed by two bright spots, corresponding to the Mn columns). Similar results were shown for $Li_{1.2}Co_{0.4}Mn_{0.4}O_2$[12] and $Li[Ni_{0.17}Li_{0.2}Co_{0.07}\ Mn_{0.56}]O_2$.[18] However, since the HAADF-STEM images are also affected (to various degrees) by the defocus value, thickness, thermal scattering factor, and aberration coefficients, STEM image simulations are necessary to verify the presence of lithium ordering. We performed STEM image simulations for both the case of a single partially ordered $C2/m$ monoclinic phase and the case of a disordered $R\bar{3}m$ structure with a small $C2/m$ region.

We first consider the case of the single partially ordered monoclinic $C2/m$ structure observed along the $\mu1$, $\mu2$, and $\mu3$ directions (Figure 4b), which correspond to the monoclinic $\pm[100]$, $\pm[110]$, and $\pm[1\bar{1}0]$ directions, respectively. These zone axes were selected because the beam is parallel to the transition-metal plane and the Mn atoms all line up in a single column, while the Ni and Li all line up together in a different column, thus facilitating the interpretation of contrast of the STEM images. Under these conditions, the projected structures along the [100] and [110] directions show that the transition-metal layer is composed of two adjacent columns of Mn separated by 0.14 nm, alternating with a column of Li/Ni (60% Li and 40% Ni) (see Figures 6a and 6b). Heavier Mn columns will appear bright in the HAADF STEM images, while the lighter

dx.doi.org/10.1021/cm200831c |Chem. Mater. 2011, 23, 3614–3621

Li/Ni-columns will appear darker. This contrast behavior is confirmed by the STEM simulations and corresponding intensity profiles shown in Figures 6c−f.

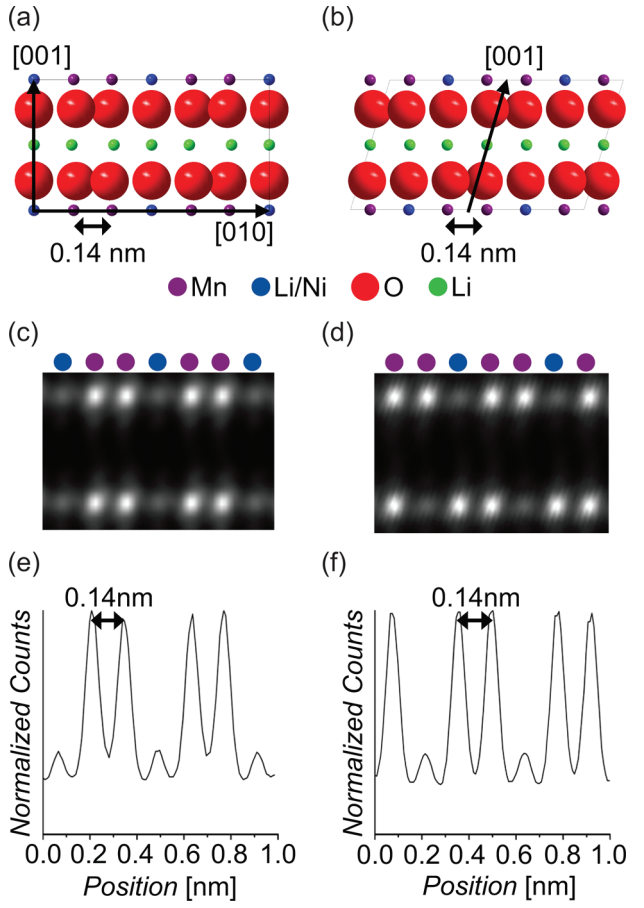

Figure 6. (a,b) Cross-sectional view of $Li[Li_{0.2}Ni_{0.2}Mn_{0.6}]O_2$ as a solid solution with partial ordering and a monoclinic ($C2/m$) unit cell viewed along the (a) [100] zone axis and (b) [110] zone axis. (c,d) Simulated HAADF/STEM images corresponding to the models shown (c) in panel a and (d) in panel b. (e,f) Intensity profiles corresponding to the image shown (e) in panel c and (f) in panel d. The value "0.14 nm" represents the distance measured in projection between the atoms; it is not the actual distance between atoms.

In the case of a disordered $R\bar{3}m$ structure having small $C2/m$ regions, each atomic column of the disordered $LiMO_2$ $R\bar{3}m$ structure projected down the equivalent $\mu1$, $\mu2$, and $\mu3$ directions in Figure 4a ($\pm[\bar{1}10]$, $\pm[210]$, and $\pm[120]$, respectively) is separated by 0.14 nm and is composed of a mixture of atoms (60% Mn, 20% Ni, and 20% Li). Hence, each column observed along any of these directions (the [120] zone axes is shown in Figure 7a as an example) should produce a series of bright columns in HAADF STEM separated by 0.14 nm, as shown by the computer simulations and corresponding intensity profile (see Figures 7b and 7c). The $C2/m$ Li_2MnO_3 structure, also oriented down the $\mu1$-axis ($\pm[100]$), shows that the transition-metal layer is composed of two adjacent columns of Mn, separated by 0.14 nm, alternating with a column of Li (see Figure 7d). Thus, the HAADF-STEM simulation and corresponding intensity profile (see Figures 7e and 7f) shows two bright columns separated by 0.14 nm, followed by a dark column. Therefore, if the $Li[Li_{0.2}Ni_{0.2}Mn_{0.6}]O_2$ composition is composed of two phases, the HAADF STEM images should show two types of areas: (i) regions with continuous bright columns separated by 0.14 nm and (ii) regions with two consecutive bright columns separated by 0.14 nm, alternating with a dark column.

The simulated STEM results can now be compared with the experimental HAADF-STEM image and the corresponding line profile shown in Figures 8a and 8b, which is observed consistently throughout the sample. As discussed in Figure 7, the disordered trigonal $R\bar{3}m$ structure cannot produce the contrast shown in Figures 8a and 8b, in which two bright atomic columns alternate with a dark atomic column. Therefore, the structure shown in Figure 8a corresponds to the partially ordered monoclinic $C2/m$ phase. The intensity between the bright columns, however, is negligible, which is not expected if 40% of the atoms along the column are Ni (see Figures 6c and 6d). Keeping in mind the fact that the thermal scattering factor (B) for the solid-solution simulations was taken from pure Li_2MnO_3, accurate quantitative values for Ni in the S_1 sites presently cannot be acquired from the simulations. However, changing B on the S_1 sites by 10% only produces a 4% change in contrast between the S_1 and S_2 sites. In fact, intensity can still be detected in the S_1 sites for the entire range of B = 0.01−1.0. Therefore, it can be concluded that the S_1 sites contain <40% Ni. In summary, the simulated and experimental STEM results show that the

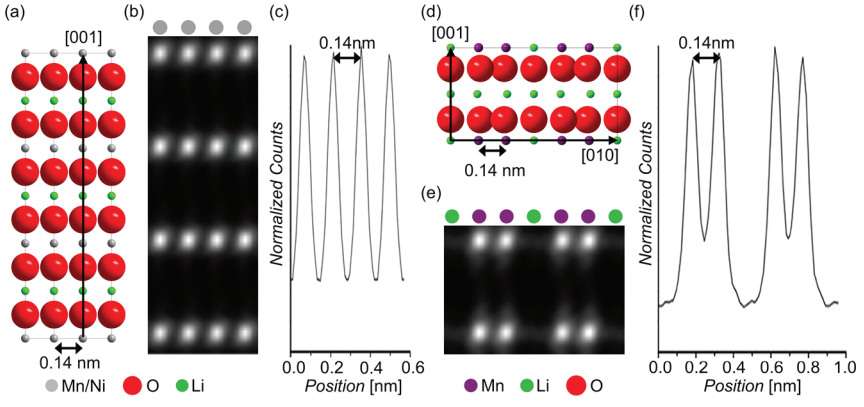

Figure 7. (a) Cross-sectional view of a unit cell of trigonal ($R\bar{3}m$) $Li[Mn_{0.5}Ni_{0.5}]O_2$ viewed along the [120] zone axis with (b) corresponding simulated HAADF/STEM images and (c) intensity profile of the simulation shown in panel (b). (d) Cross-sectional view of a unit cell of monoclinic ($C2/m$) Li_2MnO_3 viewed down the [100] zone axis with (e) corresponding simulated HAADF/STEM images and (f) intensity profile of the simulation shown in panel (e). The value "0.14 nm" represents the distance measured in projection between the atoms; it is not the actual distance between atoms.

dx.doi.org/10.1021/cm200831c |*Chem. Mater.* 2011, 23, 3614–3621

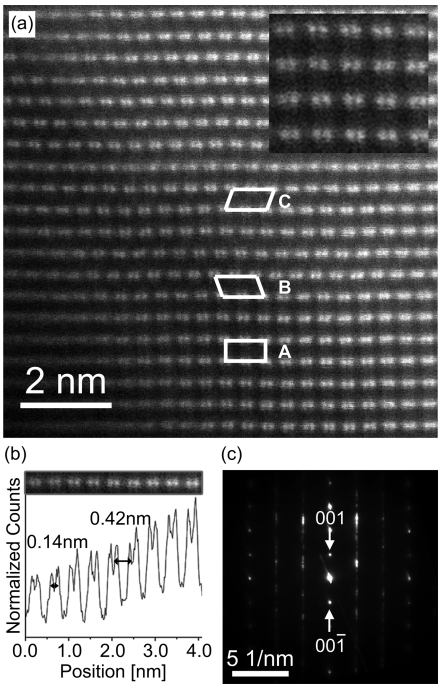

Figure 8. (a) Aberration-corrected STEM image of a Li-$[Li_{0.2}Ni_{0.2}Mn_{0.6}]O_2$ crystal; (b) intensity profile along part of one row; and (c) nanobeam electron diffraction (NBED) from another $Li[Li_{0.2}Ni_{0.2}Mn_{0.6}]O_2$ crystal. Areas marked A, B, and C in Figure 8a correspond to the [100] zone axis, the $[1\bar{1}0]$ zone axis, and the [110] zone axis, respectively.

$Li[Li_{0.2}Ni_{0.2}Mn_{0.6}]O_2$ composition is a single-phase material with $C2/m$ symmetry and exhibits significant ordering between Li^+ and the transition metal, hereafter referred to as Li ordering, in the transition-metal layers.

While Li ordering is consistent for each transition-metal layer, atomic displacements across transition-metal layers are often observed (Figure 8a). For example, region A is composed of several transition-metal layers where the Mn atoms are stacked directly on top of each other. However, for regions B and C, the Mn atoms are offset across transition-metal layers, also seen by Bareno et al.[9] and Lei et al.[14] To fully understand these atomic displacements, it is critical to interpret the NBED shown in Figure 8c, which contains multiple diffraction spots and streaking.

We first consider simulated ED patterns of the partially ordered $C2/m$ structure viewed along the [100], [110], and the $[1\bar{1}0]$ directions (see Figures 9a−c). A computer simulation of each zone axis, per se, does not match the experimental NBED. However, when the ED patterns corresponding to the [100], [110], and the $[1\bar{1}0]$ directions are superimposed (see Figures 9d and 9e), the match with the experimental data is very good. This means that, within the HAADF STEM image shown in Figure 8a, there are crystal rotations of the $C2/m$ structure. As shown in Figure 6c, the $C2/m$ structure viewed along the [100] direction produces images similar to region A in Figure 8a, whereas the $[1\bar{1}0]$ and [110] directions lead to the configurations seen in regions B and C, respectively. These results, combined with the spacing of the Mn columns in the dumbbells (0.14 nm) shown in Figure 8b, which matches the projected distances depicted in Figures 6e and 6f, confirm that the $Li[Li_{0.2}Ni_{0.2}Mn_{0.6}]O_2$ composition exhibits a partially ordered monoclinic $C2/m$ structure with crystal rotations.

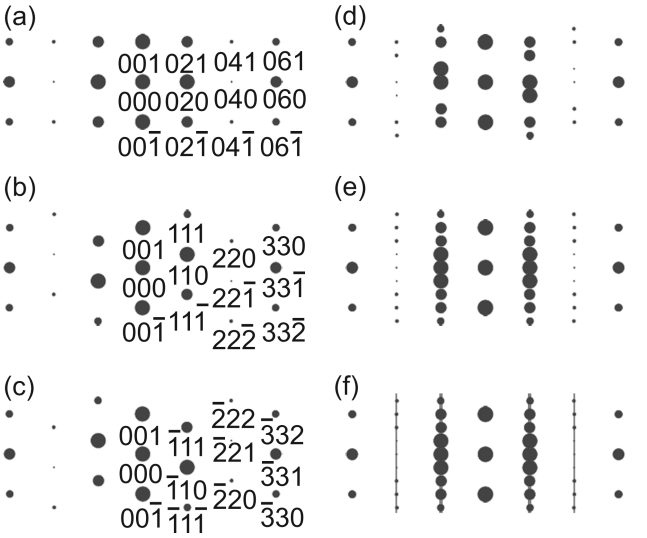

Figure 9. Simulated ED patterns from a partially ordered $C2/m$: (a) [100] zone axis; (b) $[1\bar{1}0]$ zone axis; (c) [110] zone axis; (d) [100] and $[1\bar{1}0]$ zone axes overlapped; (e) [100], [110], and $[1\bar{1}0]$ zone axes overlapped; and (f) [100], [110], and $[1\bar{1}0]$ zone axes overlapped, with streaks produced from small platelets. Patterns shown in panels (a)−(c) were acquired using the software by Zuo et al.[24] Overlapping patterns and streaking in panels (d)−(f) were constructed manually.

At this point, we are still left with one important issue, which is the appearance of streaks in the NBED along the (001) planes. A careful observation of Figure 8a shows that many of the regions of the material with a particular crystal orientation (regions A, B, and C) are just a few atomic layers thick. In other words, the structure in these regions is composed of monoclinic nanoscale platelets of different orientations, which are produced by the displacement of (001) planes along the [110] direction. As a result, streaking perpendicular to the platelets is produced, as shown in Figures 8a and 8c. Similar results were reported by Bareno et al.[9] and Lei et al.[14] This also explains the weakening and broadening of the XRD peaks (020, 110, $\bar{1}11$, and 021) in the 20°−35° range (see Figure 3), since these are the planes that contribute to streaking in the NBED pattern, because of the presence of planar defects.

As mentioned previously, the STEM simulations, HAADF/STEM experimental data, and NBED results conclusively show that the material is a solid solution with $C2/m$ symmetry. However, the STEM image shown in Figure 8a was obtained from the edge of the sample. Because of an increase in thickness, the center of the particle cannot be imaged under STEM conditions while maintaining sub-Ångström resolution. Therefore, to ensure that the sample is indeed a solid solution with $C2/m$ symmetry throughout, a series of ED patterns were obtained from multiple locations within the sample, each with an area of ~1 nm^2. For this analysis, a recent technique developed by Ganesh et al.[19] called D-STEM was used.

The D-STEM technique uses a beam configuration similar to NBED but in STEM mode. This allows for control of a 1−2 nm electron beam to be accurately positioned on the STEM image, at the region of interest, while sharp spot diffraction patterns can be simultaneously recorded on the charge-coupled device (CCD) camera. The D-STEM technique is thus very powerful for obtaining automated diffraction information acquired on a pixel-by-pixel basis. As a result, diffraction patterns can be collected from defined locations, in point, line, or area scans in

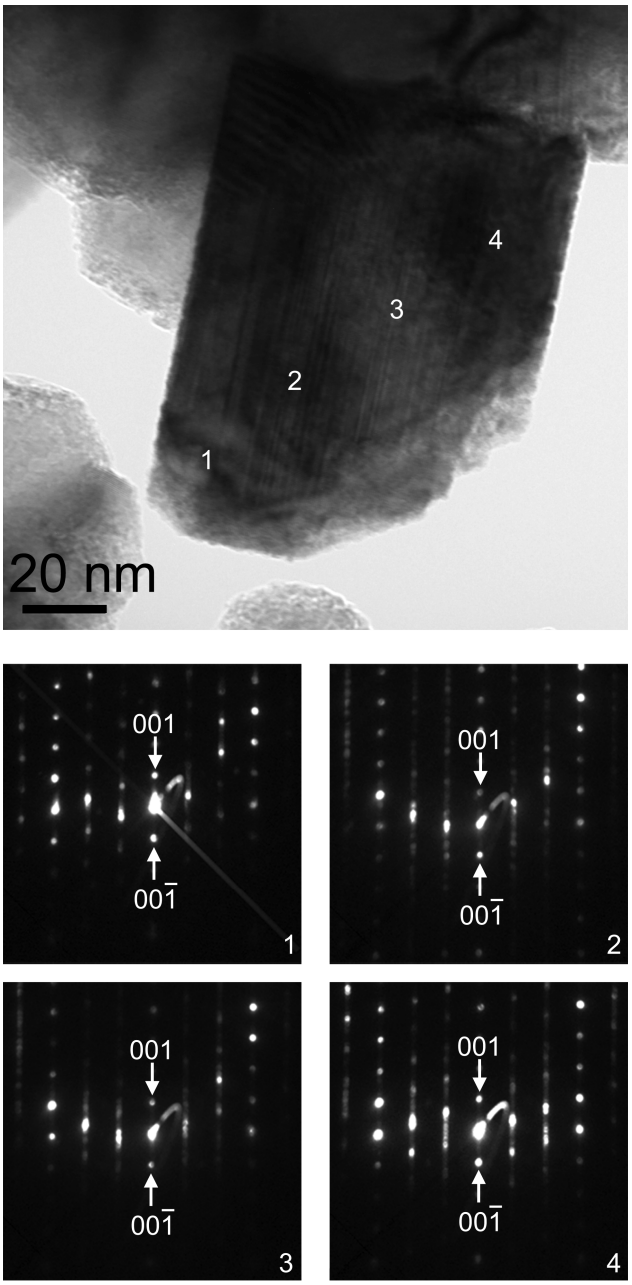

Figure 10. (Top) BF TEM image of a particle of $Li[Li_{0.2}Ni_{0.2}Mn_{0.6}]O_2$ oriented down the [100], [110], and/or [1$\bar{1}$0] directions, (Bottom) Corresponding D-STEM diffraction patterns collected at the areas indicated as 1−4 in the BF TEM image.

real time. In this fashion, we have been able, for the first time, to map ED patterns with a 1−2 nm resolution from entire particles (~1000 nm^2). On the other hand, while NBED can also collect diffraction patterns from a 1-nm region, the scanning coils of the microscope are not employed, and thus automation is not possible. Therefore, collecting diffraction data from multiple areas within a large particle is very time-consuming. In addition, in the NBED mode, it is not possible to form a small probe on the area of interest and image the sample at the same time. As a result, it is challenging to place the beam exactly on the region of interest.

Figure 10 shows a series of ED patterns acquired under the D-STEM mode and collected from different regions within the $Li[Li_{0.2}Ni_{0.2}Mn_{0.6}]O_2$ sample. Although the entire particle was scanned with a step size of 1 nm, the four patterns shown represent the overall observations seen throughout the particle. Diffraction patterns 1 and 4 in Figure 10 match well with the [1$\bar{1}$0] zone axis monoclinic pattern shown in Figure 9c, while the streaking is due to the planar defects discussed above. Patterns 2 and 3 in Figure 10 match well with the simulated ED pattern resulting from overlapping the [100], [110], and [1$\bar{1}$0] zone axes, while the streaking again represents thin planar defects (see Figure 9f). On the other hand, the diffraction patterns in Figure 10 do not match the expected pattern for $R\bar{3}m$. Hence, it can be concluded that no $R\bar{3}m$ regions exist in the sample, even at the nanoscale. The D-STEM technique was used to analyze multiple particles, and they all showed the same results. Hence, the D-STEM analysis confirms the results obtained from aberration-corrected STEM imaging, STEM simulations and NBED data, that the $Li[Li_{0.2}Ni_{0.2}Mn_{0.6}]O_2$ composition is a single monoclinic $C2/m$ phase with multiple planar defects.

CONCLUSIONS

The combination of X-ray diffraction (XRD), XRD simulations, aberration-corrected high-angle annular dark-field scanning transmission electron microscopy (HAADF/STEM), HAADF/STEM simulations, nanobeam electron diffraction (NBED), and diffraction scanning transmission electron microscopy (D-STEM) show that the compound $Li[Li_{0.2}Ni_{0.2}Mn_{0.6}]O_2$ has a monoclinic ($C2/m$) structure with Li-ordering. D-STEM, used for the first time for layered oxide materials, is especially important in revealing the absence of $R\bar{3}m$ regions. In addition, the HAADF-STEM simulations, used in conjunction with HAADF-STEM imaging and NBED, show that the compound $Li[Li_{0.2}Ni_{0.2}Mn_{0.6}]O_2$ consists of a $C2/m$ phase with a significant number of thin planar defects along the (001) planes, which lead to crystal rotations of the lattice. These thin planar defects produce intensity streaks on the electron diffraction (ED) patterns along the [001] direction and XRD peak broadening in the 20°−35° range.

This work shows that the $Li[Li_{0.2}Ni_{0.2}Mn_{0.6}]O_2$ composition does not separate into regions of $LiMO_2$ and Li_2MnO_3; instead, it forms a solid solution. Although two phases have not been observed for this compound, other compositions, especially those with less excess lithium, may result in two-phase regions, because of a lack of ordering between Li^+ and Mn^{4+} in the transition-metal layer. However, the high capacity of this class of materials cannot be attributed to the presence of two phases; therefore, this idea cannot be generalized for all Li-rich layered oxides. Now that the atomic structure and techniques for accurately determining atomic structure of a lithium-rich layered oxide material before operation have been clearly identified, future work will focus on understanding the role of the solid solution on enhancing the electrochemical properties of these materials and the behavior of these materials during cycling.

AUTHOR INFORMATION

Corresponding Author

*Tel.: 512-471-3244. Fax: 512-471-7681. E-mail: ferreira@mail.utexas.edu.

ACKNOWLEDGMENT

This material is based on work supported as part of the program, "Understanding Charge Separation and Transfer at Interfaces in

Energy Materials (EFRC:CST)", an Energy Frontier Research Center funded by the U.S. Department of Energy, Office of Science, Office of Basic Energy Sciences (under Award No. DE-SC0001091). Microscopy research at the Oak Ridge National Laboratory's High Temperature Materials Laboratory was sponsored by the U.S. Department of Energy, Office of Energy Efficiency and Renewable Energy, Vehicle Technologies Program. We gratefully acknowledge the assistance of Dr. Ji-Ping Zhou with D-STEM set up and Jacob Warneke with technical assistance for STEM simulations.

REFERENCES

(1) Kim, D.; Gim, H.; Lim, J.; Park, S.; Kim, J. *Mater. Res. Bull.* **2010**, *45*, 252.
(2) Thackeray, M. M.; Johnson, C. S.; Vaughey, J. T.; Li, N.; Hackney, S. A. *J. Mater. Chem.* **2005**, *15*, 2257.
(3) Thackeray, M. M.; Kang, S.-H.; Johnson, C. S.; Vaughey, J. T.; Hackney, S. A. *Electrochem. Commun.* **2006**, *8*, 1531.
(4) Thackeray, M. M.; Kang, S.-H.; Johnson, C. S.; Vaughey, J. T.; Benedek, R.; Hackney, S. A. *J. Mater. Chem.* **2007**, *30*, 3053.
(5) Thackeray, M. M. *J. Chem. Eng. Jpn.* **2007**, *40*, 1150.
(6) Lu, Z.; Chen, Z.; Dahn, J. R. *Chem. Mater.* **2003**, *15*, 3214.
(7) Bréger, J.; Jiang, M.; Dupré, N.; Meng, Y. S.; Shao-Horn, Y.; Ceder, G.; Grey, C. P. *J. Solid State Chem.* **2005**, *178*, 2575.
(8) Armstrong, A. R.; Holzapfel, M.; Novák, P.; Johnson, C. S.; Kang, S.-H.; Thackeray, M. M.; Bruce, P. G. *J. Am. Chem. Soc.* **2006**, *128*, 8694.
(9) Bareño, J.; Lei, C. H.; Wen, J. G.; Kang, S.-H.; Petrov, I.; Abraham, D. P. *Adv. Mater.* **2010**, *22*, 1122.
(10) Boulineau, A.; Croguennec, L.; Delmas, C.; Weill, F. *Chem. Mater.* **2009**, *21*, 4216.
(11) Boulineau, A.; Croguennec, L.; Delmas, C.; Weill, F. *Solid State Ionics* **2010**, *21*, 4216.
(12) Ito, A.; Shodo, K.; Sato, Y.; Hatano, M.; Horie, H.; Ohsawa, Y. *J. Power Sources* **2011**, *196*, 4785.
(13) Johnson, C. S.; Li, N.; Lefief, C.; Vaughey, J. T.; Thackeray, M. M. *Chem. Mater.* **2008**, *20*, 6095.
(14) Lei, C. H.; Bareño, J.; Wen, J. G.; Petrov, I.; Kang, S.-H.; Abraham, D. P. *J. Power Sources* **2008**, *178*, 422.
(15) Lei, C. H.; Wen, J. G.; Sardela, M.; Bareño, J.; Petrov, I.; Kang, S.-H.; Abraham, D. P. *J. Mater. Sci.* **2009**, *44*, 5579.
(16) Meng, Y. S.; Ceder, G.; Grey, C. P.; Yoon, W.-S.; Jiang, M.; Bréger, J.; Shao-Horn, Y. *Chem. Mater.* **2005**, *17*, 2386.
(17) Weill, F.; Tran, N.; Croguennec, L.; Delmas, C. *J. Power Sources* **2007**, *172*, 893.
(18) Wen, J. G.; Bareño, J.; Lei, C. H.; Kang, S.-H.; Balasubramanian, M.; Peterove, I.; Abraham, D. P. *Solid State Ionics* **2011**, *182*, 98.
(19) Ganesh, K. J.; Kawasaki, M.; Zhou, J. P.; Ferreira, P. J. *Microsc. Microanal.* **2010**, *16*, 614.
(20) Shao-Horn, Y.; Hackney, S. A.; Armstrong, A. R.; Bruce, P. G.; Gitzendanner, R.; Johnson, C. S.; Thackeray, M. M. *J. Electrochem. Soc.* **1999**, *146*, 2404.
(21) Dyer, L.; Borie, B. S.; Smith, G. P. *J. Am. Chem. Soc.* **1954**, *76*, 1199.
(22) Johnston, W. D.; Heikes, R. R.; Sestrich, D. *J. Phys. Chem. Solids* **1958**, *7*, 1.
(23) Strobel, P.; Labert-Andron, B. *J. Solid State Chem.* **1988**, *75*, 90.
(24) Zuo, J. M.; Mabon, J. C. *Microsc. and Microanal.* **2004**, *10(Suppl. 2)*, URL: http://emaps.mrl.uiuc.edu/.
(25) Ishizuka, K. *Ultramicroscopy* **2001**, *90*, 71.
(26) Weickenmeier, A.; Kohl, H. *Acta Crystallogr., Sect. A: Found. Crystallogr.* **1991**, *A47*, 590.
(27) Howie, A. *J. Microsc.* **1979**, *117*, 11.